 doi:10.20944/preprints202107.0277.v1

Article

Detection of Cervical Cancer Cells in Whole Slide Images Using Deformable and Global Context Aware Faster RCNN-FPN

Xia Li[1], Zhenhao Xu[1], Xi Shen[1], Yongxia Zhou[1], Binggang Xiao[1], Tie-Qiang Li[1,2,3*]

[1] Institute of Information Engineering, China Jiliang University, 258 Xueyuan Street, Xiasha Higher Education Zone, 310018 Hangzhou, China
[2] Department of Clinical Science, Intervention and Technology, Karolinska Institutet, S-17177 Stockholm, Sweden, tie-qiang.li@ki.se
[2] Department of Medical Radiation and Nuclear Medicine, C2-76, Karolinska University Hospital, Huddinge S-141 86 Stockholm, Sweden, tie-qiang.li@ki.se
* Correspondencetie-qiang.li@ki.se; Tel.: +46 858 580 888

Simple Summary: A novel framework based on Faster RCNN-FPN architecture has been proposed for the detection of abnormal cells in whole slide images from cervical Pap smear test. Experimental results demonstrate that the proposed framework outperforms other state-of-the-art object detectors. Particularly, when combined with tagging of the negative image samples using traditional computer-vision techniques, 6-9% improvement in mAP has been achieved.

Abstract: Cervical cancer is a worldwide public health problem with a high rate of illness and mortality among women. In this study, we proposed a novel framework based on Faster RCNN-FPN architecture for the detection of abnormal cervical cells in cytology images from cancer screening test. We extended the Faster RCNN-FPN model by infusing deformable convolution layers into the feature pyramid network (FPN) to improve scalability. Furthermore, we introduced a global contextual aware module alongside the Region Proposal Network (RPN) to enhance the spatial correlation between the background and the foreground. Extensive experimentations with the proposed deformable and global context aware (DGCA) RCNN were carried out using the cervical image dataset of "Digital Human Body" Vision Challenge from the Alibaba Cloud TianChi Company. Performance evaluation based on the mean average precision (mAP) and receiver operating characteristic (ROC) curve has demonstrated considerable advantages of the proposed framework. Particularly, when combined with tagging of the negative image samples using traditional computer-vision techniques, 6-9% increase in mAP has been achieved. The proposed DGCA-RCNN model has potential to become a clinically useful AI tool for automated detection of cervical cancer cells in whole slide images of Pap smear.

Keywords: Cervical cancer; Pap smear test; whole slide image (WSI); feature pyramid network (FPN); global context aware (GCA); region based convolutional neural networks (R-CNN); Region Proposal Network (RPN).

 doi:10.20944/preprints202107.0277.v1

1. Introduction

Cervical cancer is the second most common malignancy among women with more than half a million new cases reported annually. It can be detected and prevented at its early stage by cytology screening test. Over the last 6 decades cervical smear of Pap strains has played an important role in controlling cervical cancer epidemic by detecting pre-cancerous changes and providing guidance for early treatments. It was estimated that Pap smear test can reduce mortality rate by 70% or more[1]. Cytological slides of vaginal smear of Pap strains are microscopically examined at 400× magnification. With such magnification, cytologists must examine thousands of field-of-views (FOVs) per slide and, thereby, are limited to investigate a limited number of samples per day. Despite the seemingly simplicity in detection of abnormal cervical cells, experienced physicians are required for an accurate diagnosis and there is a lack of such healthcare resource in many developing countries. Moreover, even with experienced pathologists, it is a tedious task to examine the pap smear slides through microscope and the detection of cervical cancer cells can often be missed, due to the small size of the cervical intraepithelial neoplasia, overlapping clump of cells or masking by blood mucus and artifacts.

In the light of these challenges, different computer-aided diagnosis technologies have been proposed [2-5] to reduce the workload of pathologists and improve the efficiency and accuracy of cervical cancer detection. The computer-assisted screening for cervical cancer cells involves typically into two steps: segmentation [6] of cytoplasm and nucleus, and classification[7]. After the entire image is segmented into nuclei and cytoplasm, these small pieces are classified into abnormal and normal ones, and finally used for the diagnosis of cervical cancer. The segmentation quality is, therefore, vital for the extraction of cell features and the consequential classification results. This has been a subject of extensively investigation[6,8-15] in the last 2 decades. Cell overlapping is one of the difficulty issues for accurate cell segmentation and effective methods to separate overlapping cells have been proposed[11,16-18]. After successful segmentation into individual cells, the performance for cell classification relies on the extraction of morphological, structural, and contextual features and optimal selection of classifiers [19]. Due to the complicated characteristics of cervical cells and pathological subtleties associated with cervical cancer development, traditional computer vision methods can only provide limited generality and efficiency for segmentation and feature extraction.

With the advent of deep learning based artificial intelligence (AI) technology in recent years, particularly, the development of convolutional neural networks (CNNs) has demonstrated its potential for improving automated cervical cancer screening and diagnosis. Deep learning excels at recognizing patterns and high-level sematic features in large volumes of data, extracting relationships between complex features in the images, and identifying characteristics that is difficult be perceived by the human brain. AI software can process vast number of images rapidly and has already been used to assist clinicians in level classification of skin cancer[20], breast cancer detection[21,22], end-to-end lung cancer screening [23] and prediction of colorectal cancer outcomes[24]. Significant progress has also been made in automated cervical cancer classification. With these classification methods we leverage the deep CNNs for effective extraction of deep and high-level features [3,7,25-31] of the cells to achieve more accurate cancer screening.

Deep learning technology has also led to breakthroughs in object detection, which refers to the task of both identifying the locations and categorizing object instances in images. Object detection is a key ability required by most computer and robot vision systems. The cutting-edge research in the field has been making amazing

 doi:10.20944/preprints202107.0277.v1

progress in many directions, such as automatic car-driving and object tracking. Current object detection models can be divided into two main categories, proposal-driven two-stage detectors, and proposal-free single stage detectors. For the two-stage detectors, such as faster region-based CNN (FRCNN) series[32-35], region-based fully convolution network (R-FCN)[36], and feature pyramid network (FPN) [33], the detection process is completed in two steps. First the algorithms produce sparse candidate proposals, and then further refine the coordinates and classify these candidate proposals. The two-stage methods generally have higher accuracy at the cost of speed. In contrast, the one-stage detectors generate the object's category labels and locations directly and have advantage in speed, such as YOLO [37] for real-time object detection, single shot multibox detector (SSD) series [38] and RetinaNet[39]. More recently, a new category of anchor-free single-stage detectors has emerged[40], which has completely abandoned the anchor mechanism.

The object detection methods have also begun to find applications for cervical cancer detection in cervical cytology images. At present, there are few network architectures designed specifically for the specific task of cervical cancer detection [41-46]. Xu et al. [45] used the generic Faster RCNN for the detection of abnormal cells in cervical smear images scanned at 20× and showed that detection of various abnormal cells was feasible. Zhang et al.[46] tested a R-FCN model for cervical cancer screening of liquid based cytology (LBC) images. Their performance evaluation was based on an interesting concept called hit degree which ignores the precise IOU threshold, and a hit recall was counted if the ground truth boxes hit by any detection result box. Accordingly, the precise positions of the cell nuclei are less important because the cells tend to form clumps in the Pap smear slides. Tan et al.[44] used also Faster RCNN architecture for cervical cancer cell detection in ThinPrep cytologic test (TCT) images scanned with a seamless slider at up to 400× and achieved AUC of 0.67. More recently, Ma et al.[42] proposed an improved Faster RCNN-FPN architecture for cervical cancer detection in cropped patches out of positive Pap smear images. They designed a lightweight booster consisting of a refinement and spatial-aware module, aimed to enhance feature details and spatial context information.

As discussed above, the automated detection of cervical cancer cells in the cytology images is a multi-task process involving feature extraction, cell localization, and classification. Although extensive research efforts in the past have made significant progress in automated classification and detection of the abnormal cervical cells, some bottle neck issues remain still open. Particularly relevant concerns include the following: (1) the abnormalities in the cancerous cells are subtle and complex; (2) Cells in the cervical Pap smear images exist in different sizes and their geometric shapes can be obscured due to clump formation and overlapping with artifacts; (3) The ROI pooling/aligning processes in the object detection algorithms tend to enhance the local receptive fields and lose global context information.

Aimed at mitigating these potential limiting factors for more accurate detection of abnormal cells in cervical cytology images, in this study, we introduce two functional extensions for one of the top-performing object detectors, the Faster RCNN-FPN framework: One is the infusion of deformable convolution network (DCN)[47-51] in the last 3 stages of the bottom-up pathway of the FPN and the other is adding global context aware (GCA) module[52] alongside the RPN. A unique advantage of the Faster RCNN-FPN architecture is its inherent multi-scale nature in feature extraction and can facilitate the cell detection of different sizes. Infusion of the deformable convolution layers into the later 3 stages of the FPN structure can explicitly learn the geometric offset information of the objects associated with shape transformations. we added GCA module into the Faster RCNN-FPN to strengthen the spatial correlation between the background and foreground. In the GCA module, the feature pyramid and attention

Preprints (www.preprints.org) | NOT PEER-REVIEWED | Posted: 12 July 2021 doi:10.20944/preprints202107.0277.v1

strategies are used for global feature extraction and feature refinement, respectively. We leverage the extracted global features as attention maps for contextual modulation to improve the cell detection performance. Moreover, we utilize various conventional computer-vision techniques for imaging process to preprocess the negative image samples and tag some of the representative cells aimed to enhance the subtle feature differences between the negative and positive cancerous cells. We conducted extensive experiments using the dataset from the "Digital Human Body" (DHB) Vision Challenge (tianchi.aliyun.com/competition/entrance/231757/information) with the proposed deformable and global context aware (DGCA) Faster RCNN-FPN architecture (hereon abbreviated as DGCA-RCNN). Besides exhaustive test, we evaluated the performance of the proposed DGCA-RCNN framework and conducted systematic performance comparison with five other state-of-the-art object detectors including ATSS[53], RetinaNet[39], Faster RCNN-FPN[34], double-head[54], and Cascade RCNN[32]. We carried out also abolition analysis of the extensions in the DGCA-RCNN framework to access their functional importance for the detector's performance.

2. Materials and Methods

2.1. The proposed framework for cervical cancer cell detection

Figure 1 depicts the architecture details of the proposed DGCA-RCNN framework. It is based on the faster RCNN-FPN architecture consisting of image input, feature pyramid network (FPN) for feature extraction, feature map generation with region proposal network (RPN), classifier, and bonding box regressor. As shown in Figure 1, the FPN consists of a bottom-up and top-down pathways. The bottom-up pathway is a deep convolutional network hierarchy for feature extraction with successively decreasing spatial dimension. As more high-level features are extracted, the semantic value for each layer increases. The bottom layers (C1) are not included for object detection because of their limited semantic value and large dimension. They are in high resolution, require too much memory and can result in significant slowdown. The framework only uses the upper layers for detection and, therefore, performs much worse for smaller objects. However, FPN also provides a top-down pathway to construct higher resolution layers from a semantic rich layer using up-samplings. While the reconstructed layers are semantically strong, locations are not precise after all the down- and up-samplings. Therefore, lateral connections between the reconstructed layers and the corresponding feature maps are utilized to generate pixelwise addition to improve the localization precision. They also act as skip connections to facilitate training.

In this study, we used ResNet-50 to construct the bottom-up pathway. It composes of 5 convolution modules (C1-C5) and each has multiple convolution layers. From C1 to C5 the spatial dimension is reduced by ½ at each stage. We apply a 1×1 convolution filter to reduce the C5 channel depth to 256-d (P5). This becomes the first feature map layer used for object prediction. Along the top-down route, the previous layer is up-sampled by a factor of 2 using the nearest neighbor up-sampling method. The up-sampled P5 was added with the 1x1 filtered C4 pixel-wise to generate P4. The same process is repeated to generate P3 and P2. In this way, the FPN network utilizes its inherent multi-scale pyramidal hierarchy of deep convolutional networks to construct feature pyramids and make independent predictions at different levels (P2, P3, P4, P5 and P6) for multi-scale object detection. The RPN network loops through the different prediction levels and makes full use of the feature maps of different scales at 32×32, 64×64, 128×128, 256×256, and 512×512, respectively. Furthermore, three aspect ratios of 1:1, 1:2 and 2:1 are utilized at each level. The RPN is trainable from end-to-end to generate simultaneously bounding-box proposals and objectness scores at each position. These regions may contain target objects and are sent to the subsequent classifier network to produce the final classification and refined anchor positions. Since the same classifier/regressor model is shared among the region proposals from the feature map pyramid of different

Preprints (www.preprints.org) | NOT PEER-REVIEWED | Posted: 12 July 2021 doi:10.20944/preprints202107.0277.v1

levels, the region of interest (ROI) pooling layer uses max pooling to convert each ROI from the RPN into a feature map of fixed size at 7×7.

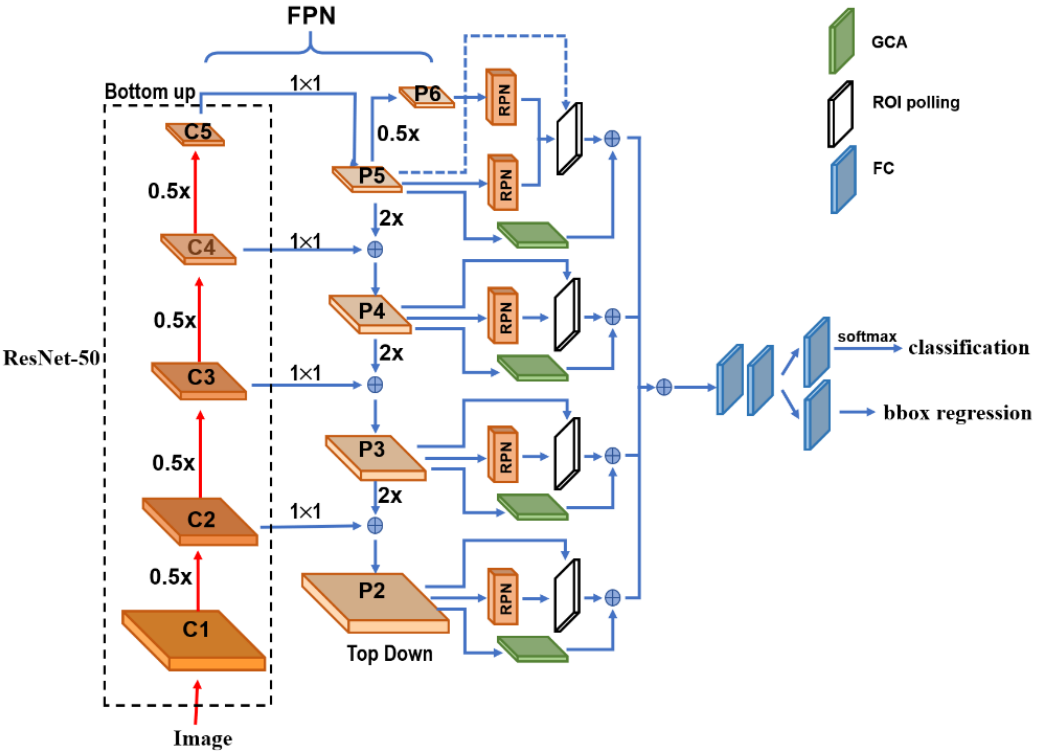

Figure 1. A schematic illustration of the proposed DGCA-RCNN architecture.

2.2. Extensions to the Faster RCNN-FPN architecture

The regular grids are used in the input feature maps for the convolution operations and CNNs are limited in modeling geometric transformations. Introducing deformable convolutional layers can add 2D offsets to the regular grid sampling locations in the standard convolution and can facilitate the detection of the geometrically transformed objects without additional supervision[55]. Considering the geometrical variations of diploids in the cervical smear images, we replaced the last convolution layers in C3, C4, and C5 of the ResNet-50[56] backbone by deformable convolutional layers in the proposed framework. With the extension we can obtain the field offsets to model the various geometrical deformations of the cells on top of their ordinary feature maps. During training, both the convolutional kernels for generating the output features and the field offsets can be learned simultaneously. Therefore, we expect to improve the generality of the model in the aspects of scalability, geometry transformation and cell deformation.

As discussed above, ROI Pooling/Aligning is an indispensable process for the Faster RCNN-FPN architecture. It is used to rescale the object proposals cropped from the feature pyramid to generate a fixed-size feature map. However, these cropped feature maps of dominant local receptive fields possess very weak global context information. To alleviate this, we infuse an off-the-shelf Global Context Aware (GCA) module to strengthen the spatial correlation between the background and foreground by fusing the global context information through attention mechanism. We leverage the extracted global features as attention maps for contextual modulation to improve the cell detection. In the end, the GCA module also utilizes a max pooling to convert the global context features at different stages in the top-down route of FPN into the fixed size of 7×7 and merges them pixel-wise with the ROIs from ROI pooling layer. The reference information from the background may help decide the spatial and category relationship between the targets and global contexts.

2.3. the loss functions

Preprints (www.preprints.org) | NOT PEER-REVIEWED | Posted: 12 July 2021 doi:10.20944/preprints202107.0277.v1

The loss function of the detection algorithm can be divided into two parts, one is the RPN loss, and the other is the loss of the detection network. To evaluate the RPN loss, we used the intersection-over-union (IOU) metric which is defined as the ratio between the area of overlap and the area encompassed jointly by both the predicted bounding box and the ground-truth bounding box. Depending on the associated IOU each anchor is assigned a binary class label. If the IOU for a given anchor is >0.7 or <0.3, positive or negative label will be signed to the anchor, respectively. The detection model is optimized for a loss combining the two tasks: classification and localization. Therefore, the loss (L) function sums up the cost of classification (L_{cls}) and bounding box prediction (L_{box}):

$$L = L_{cls} + L_{box} \quad (1)$$

$$L(\{p_i\},\{t_i\}) = \frac{1}{N_{cls}}\sum_i L_{cls}(p_i, p_i^*) + \frac{\lambda}{N_{box}}\sum_i p_i^* \bullet L_1^{smooth}(t_i - t_i^*) \quad (2)$$

where L_{cls} is the log loss function over two classes (positive and negative), as we can easily translate a multi-class classification into a binary classification by predicting a sample being a target object versus not.

$$L_{cls}(p_i, p_i^*) = -p_i^* \log p_i - (1-p_i^*)\log(1-p_i) \quad (3)$$

The bounding box loss L_{box} should measure the difference between t_i and t_i^* using a robust loss function. The smooth L_1 loss is adopted here as usual, and it is claimed to be less sensitive to outliers.

$$L_1^{smooth}(x) = \begin{cases} 0.5x^2 & if\ |x| < 1 \\ |x| - 0.5 & otherwise \end{cases} \quad (4)$$

Other symbols' definitions in the above equations are provided in Table 1.

Table 1. Definitions of the symbols used in the loss functions.

Symbol	Explanation
i	The index of anchors in a mini batch.
p_i	Predicted probability of anchor *i* being an object.
p_i^*	Ground truth label (binary) of whether anchor i is an object.
t_i	Predicted four-parameter coordinates for anchor *i*.
t_i^*	Ground truth coordinates.
N_{cls}	Normalization term, set to be mini-batch size (~256).
N_{box}	Normalization term, set to the number of anchor locations,
λ	A balancing parameter, set to be ~10, so that both L_{cls} and L_{box} terms are roughly equally weighted.

2.4. The Dataset and Preprocessing pipeline

For the study we used the cervical cytology image dataset from "Digital Human Body" (DHB) Vision Challenge-Intelligent Diagnosis of Cervical Cancer Risk provided by the Alibaba Cloud TianChi Company (https://tianchi.aliyun.com/competition/ entrance/231757/ information?scm=20140722.184.2.173). The original images were in KFB format and acquired with digital scanning under 20x magnification. Typical file size is in the range of 300-400MB. The dataset contains 500 positive and 300 negative whole slide images (WSI) of 40,000x40,000. The positive WSIs have marked ROIs where the positions of 5414 lesions with abnormal squamous epithelial cells were labeled. The coordinate and size information for the ROIs were provided in an associated list document in json format. The abnormal squamous epithelial cells include mainly four types: atypical squamous cells (ASC-US) which cannot be clearly defined, low-grade intraepithelial lesions (LSIL), atypical squamous cells (ASC-H) which tend to have high intraepithelial cells, and high intraepithelial lesions (HIS). It is notable that there is no guarantee that there is no abnormal squamous epithelial cell outside the marked ROIs for the positive WSIs.

Preprints (www.preprints.org) | NOT PEER-REVIEWED | Posted: 12 July 2021 doi:10.20944/preprints202107.0277.v1

We utilized a library package provided by Ningbo Jiangfeng Konfoong Bioinformation Tech Co.,Ltd (https://www.exporthub.com/eh-ningbo-konfoong-bioinformation-tech-co-ltd/) to convert from KFB to PNG format which has 3-channel RGB and 8-bit depth in each channel. Due to the limited GPU memory, the WSIs cannot be fed into the model directly and were cropped into smaller patches. As illustrated in Figure 2, for the training dataset we cropped all the marked ROIs in each positive WSI using a sliding window method to extract systematically patches of 2000×2000 out of each ROI. The overlap of the sliding window was 50% in both directions., On average, about 20 patches were generated per positive sample. reference information from the background may help decide the spatial and category relationship between the targets and global contexts.

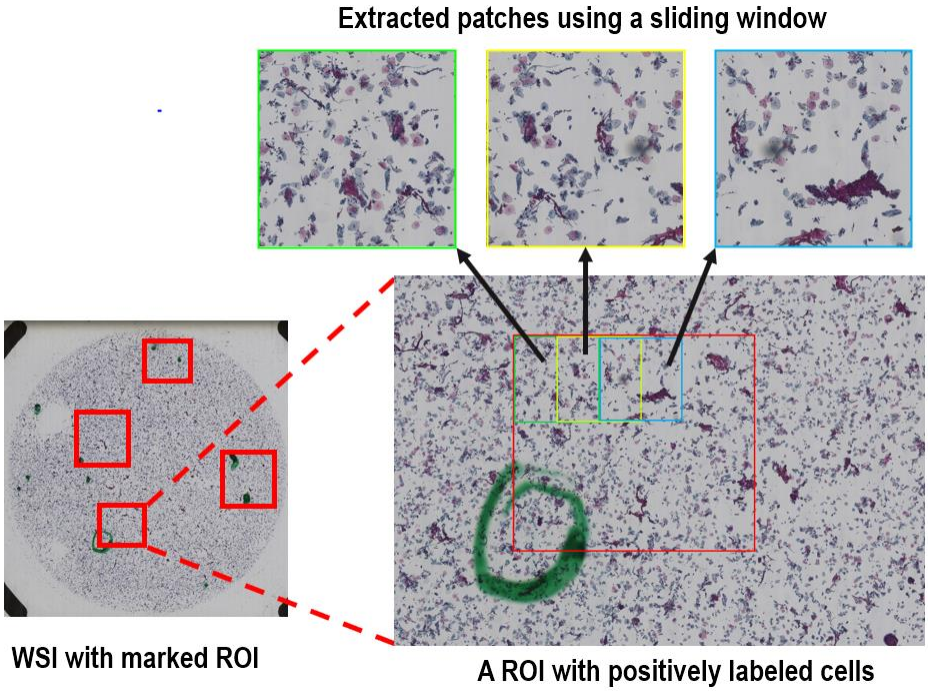

Figure 2. The preparation procedure for the positive WSIs to extract image patches of 2000 × 2000 out of the labeled ROIs using a sliding window with 50% overlap.

For the negative samples without any specified ROI and the test dataset of the positive samples, we used the same sliding window method to crop the entire region within the radius of 20,000 voxels from the center of each WSI, because a statistical analysis of the marked ROIs for the positive samples showed that all positively labeled cells were within this range. There are rarely any cells at the edge of the images.

To enhance the features in the negative image samples, we applied computer-vision techniques to label some of the negative cells. The negative tagging can improve the performance of the model and further reduce the false positive rate. As schematically illustrated in Figure 3, the procedure to label the negative cells included the following steps: Firstly, the RGB images were color averaged to generate grayscale images which were denoised using a series of filters. Then corrosion and dilation operations were applied to the binarized images before edge detection using the canny algorithm. Finally, for each of the preprocessed image patch a few cells of appropriate sizes were selected in a pseudo-random fashion and labeled as negative cells. The selection of the negative cells was carried by using a random number generator after ranking the edge-detected negative cells according to their areas. The total number of the extracted image patches with negatively labeled cells was controlled to be the same as that for the positively labeled image patches (see Table 2).

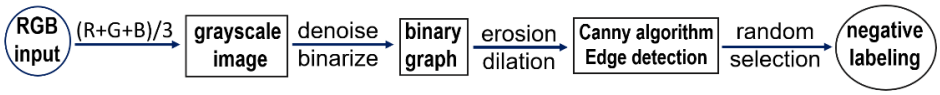

Preprints (www.preprints.org) | NOT PEER-REVIEWED | Posted: 12 July 2021 doi:10.20944/preprints202107.0277.v1

Figure 3. Summary of the traditional image preprocessing procedure used to select and label some of the cells in the negative image samples.

To assess the performance of the trained model, we picked 80 positive and negative samples as the test dataset in a pseudo-random fashion. The rest of dataset including both the positive and negative cases were used to train the proposed DGCA-RCNN model. The test dataset was also cropped by using the same sliding window described above to crop systematically each WSI within the radius of 20,000 voxels. The details of training and test datasets are summarized in Table 2.

Table 2. The number of WSIs and cropped patches for the training and test datasets.

Category	Positive		Negative	
	WSI	patch	WSI	patch
Training set	420	7801	220	7801
Test set	80	104972	80	122560

we performed the standard data augmentation procedure by adding image rotations and adjustment of the overall brightness. Rotations were performed three times on each image with a step size of 90°. Rotation may slightly alter the image quality but should not change the abnormality or normality of the cells. The overall image brightness was changed by about ±20%. The slightly darkening or brightening the entire FOV should not affect the detection results. Changing the brightness of the images can replicate the clinical conditions of different image qualities and stain settings in preparing the slides. Zero-mean normalization to attain centralization of the input data was also implemented for each RGB channel. This can improve the generality of the model by reducing the interference from settings, such as the staining conditions and imaging equipment.

2.6 The implementation and training procedure of the models

We implement the DGCA-RCNN model using PyTorch (version 1.8.1). for the Python environment (version 3.5). The training and test of the model were carried out on a GPU server equipped with 4 NVIDIA TITAN X (Pascal) with 12GB GPU memory. For comparison, based on the same backbone of ResNet50, we also implemented other five closely related the state-of-the-art object detection models developed in recent years including ATSS[53], RetinaNet[39], Cascade RCNN[32], Double head[54], and Faster RCNN-FPN[57]. We compared these models by strictly ruling out all the implementation inconsistencies between them.

We used the alternating training strategy to train the model, the RPN was first trained to generate the initial region proposals. The weights of the shared convolutional layers were initialized based on the pre-trained model using ImageNet. The other weights of the RPN were initialized randomly. The generated region proposals by the RPN were then used to train the Faster RCNN model. The weights of the shared convolutional layers are then initialized with the tuned weights by the RPN. The other Faster R-CNN weights were initialized randomly. When the weights for Faster RCNN and the shared layers were tuned, the tuned weights in the shared layers were again used to train the RPN, and the process repeats iteratively until convergency. In the initial stage, we used a warm-up strategy to attain learning stability and in the final stage we adopted a scheme of multi-step decay to improve convergency. The entire scheme of learning rate adjustment to train the model is depicted in Figure 4. In the first 500 iterations, the learning rate was linearly increased to 0.005. Then, the learning rate

Preprints (www.preprints.org) | NOT PEER-REVIEWED | Posted: 12 July 2021 doi:10.20944/preprints202107.0277.v1

was kept flat in the next 7500 iterations. The ramp-down epochs were completed in 3-steps by reducing the learning rate by a factor of 10 in each step.

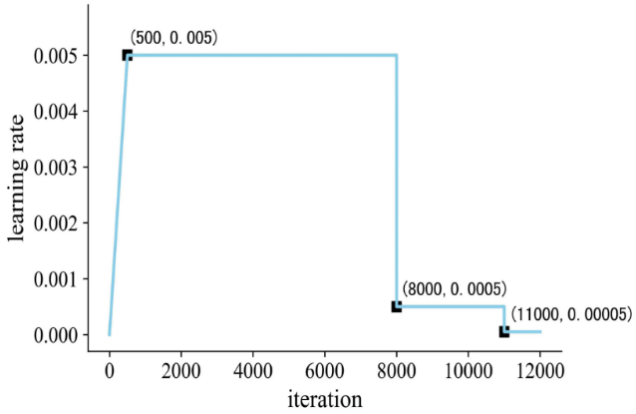

Figure 4. The scheme of learning-rate control used to train the proposed DGCA-RCNN model.

We also conducted abolition experiments with the proposed model to analyze the performance contributions from the different components, particularly the deformable convolution layers, GCA model and labeling of the negative samples.

2.6 Evaluation Metrics to assess the performance of the models

When the IOU between the predicted and the ground truth bounding box exceeds a specified threshold value, it is considered as a correct detection. Depending on the specified confidence threshold, the detection results can have 4 possible types of outcomes: true positive (TP), false positive (FP), true negative (TN) and false negative (FN). Based on the detection results, the performances of the tested models are assessed using the following metrics:

Precision (P) is the model's ability to identify only the relevant objects and is defined as the percentage of correct positive predictions among all positive detections:

$$P = \frac{TP}{Total\ positive\ detection} = \frac{TP}{(TP+FP)} \tag{5}$$

Recall (R) is the model's ability to detect all the relevant cases and defined as the percentage of the true positives among all positive ground truth cases:

$$R = \frac{TP}{Total\ pcancer\ cases} = \frac{TP}{(TP+FN)} \tag{6}$$

Both precision and recall metrics are important for object detection, it is, therefore, necessary to determine the precision-recall curve that shows the tradeoff between the precision and recall values for different thresholds. Furthermore, with the precision-recall curve the average precision (AP) can be estimated, which is a widely used metric to access the accuracy of an object detector. AP computes the average precision value for recall value over 0 to 1. The general definition for AP is to estimate the area under the precision-recall curve. That is

$$AP = \int_0^1 P(R)\, dR \tag{7}$$

Preprints (www.preprints.org) | NOT PEER-REVIEWED | Posted: 12 July 2021 doi:10.20944/preprints202107.0277.v1

In practical calculation of AP, the precision-recall curve, P(R), is usually interpolated into multiple discrete points. For a set of queries (n), the mean average precision (mAP) is computed as follows:

$$mAP = \frac{1}{n}\sum_{k=1}^{k=n} AP_k \quad (8)$$

where k is the query index in the set and APk is the average precision for a given query k. In this study, we adopted the latest MS Common Objects in Context (COCO) method and a 101-point interpolated AP definition was used in the calculation for three different IOU thresholds. Besides the metrics outlined above, other metrics, such as specificity, sensitivity, and area under curve (AUC) of the receiver operating characteristics (ROC) are also commonly used along for evaluating detection models. The ROC is a graph of the relationship between the true-positive rate (sensitivity) and the false-positive rate (1-specificity), which measures the effects of varying decision thresholds and accounts for all possible combinations of various correct and incorrect detections. Both mAP and AUC for the test set were computed for the following three IOU thresholds: 0.1, 0.3 and 0.5.

3. Results

The number of parameters and frame per second (FPS) for the different models are summarized in Table 3.

Table 3. The number of parameters and FPS for the different models.

Model	Parameters	FPS
ATSS [53]	31.89MB	3,5
RetinaNet [39]	36.6MB	3,7
Cascade RCNN [32]	68.93MB	3.1
Double head [54]	47.3MB	2.1
Faster RCNN-FPN [57]	41.53MB	3,6
DGCA-RCNN	42.11MB	3.3

Compared with the closely related model Faster RCNN-FPN, the proposed DGCA-RCNN model does non introduce significant overhead in terms of model complexity and computation burden. The number of parameters and time efficiency as indicated by FPS are quite comparable.

The results for the test dataset indicate that the proposed DGCA-RCNN framework can improve the detection performance for cervical abnormal cells at all tested 3 IOU thresholds compared with the other state-of-the-art models based on the same backbone ResNet50. As shown in Tables 4 and 5, the DGCA-RCNN model achieved the highest mAP and AUC at all IOU thresholds. Faster RCNN-FPN has the next best performance. Compared with the closely related model, Faster RCNN-FPN, the mAP for the DGCA-RCNN model is boosted by 7-9% depending on the IOU threshold, while AUC is increased by 1-2%. As expected, the performance degrades with the increasing IOU thresholds and the corresponding mAP values are systematically reduced (see Table 4). A similar trend has also been observed for the AUC results (Table 5).

Preprints (www.preprints.org) | NOT PEER-REVIEWED | Posted: 12 July 2021 doi:10.20944/preprints202107.0277.v1

Table 4. Comparison of the mAP at three different IOU levels for the proposed DGCA-RCNN framework with other state-of the-art methods for object detection.

Model	mAP@0.1	mAP@0.3	mAP@0.5
ATSS [53]	0.362	0.354	0.329
RetinaNet [39]	0.374	0.363	0.341
Cascade R-CNN [32]	0.385	0.38	0.355
Double head [54]	0.388	0.382	0.355
Faster RCNN-FPN [34]	0.415	0.394	0.371
DGCA-RCNN	0.505	0.486	0.445

Table 5. The AUC results for the ROC curves at three different IOU thresholds.

Model	ROC @0.1	ROC @0.3	ROC @0.5
ATSS [53]	0.603	0.562	0.503
RetinaNet [39]	0.633	0.584	0.526
Cascade RCNN [32]	0.653	0.609	0.548
Double head [54]	0.522	0.489	0.446
Faster RCNN-FPN [34]	0.652	0.610	0.557
DGCA-RCNN*	0.670	0.625	0.569

Table 6 shows the abolition results for the proposed model assessed at patch level for 3 different IOU thresholds. The mAP has been steadily boosted by proposed extensions. Introducing deformable convolution layers improved mAP by 2.8-4.5%. The effect of introducing GCA module is quite inconsequential for mAP (0.1-0.6%), but nevertheless the effect is positive. The tagging of the negative image samples with computer vision techniques made significant improvement in mAP by 2.1-4.9%. To better understand this effect, we carefully compared the detection results with and without the tagging of the negative samples.

Table 6. The abolition results for the proposed DGCA-RCNN model at 3 different IOU thresholds. The contributions associated with DCN, GCA and tagging of negative samples were analyzed.

Scale	DCN	GCA	Negative	$mAP_{0.1}$	$mAP_{0.3}$	$mAP_{0.5}$
Patch				0.415	0.394	0.371
	√			0.461	0.439	0.399
	√	√		0.467	0.445	0.396
	√	√	√	0.505	0.486	0.445

A clear observation is that the negative tagging reduces false positive detections. Figure 5 shows such an example without (Figure 5A) and with (Figure 5B) the use of tagging the negative image samples. With the additional labeling information from the negative images, some subtle features of the negative cells appear to be enhanced and lead to reduced false positive detections, particularly in regions with clusters of nuclei.

Preprints (www.preprints.org) | NOT PEER-REVIEWED | Posted: 12 July 2021 doi:10.20944/preprints202107.0277.v1

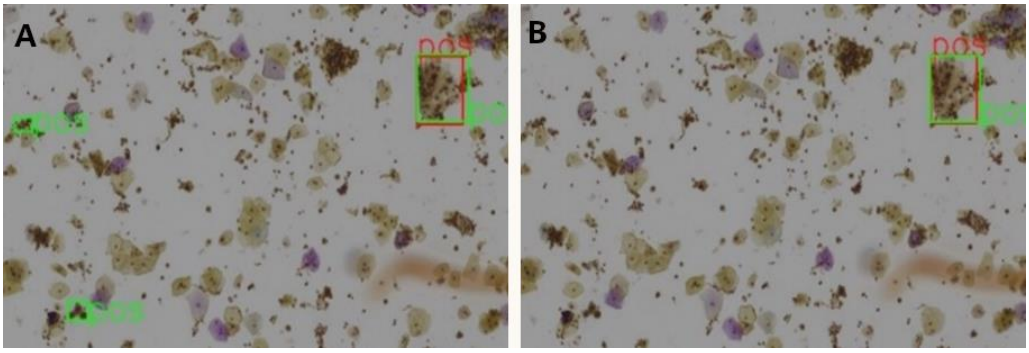

Figure 5. A zoomed display for the detection results without (A) and with (B) tagging of the negative image samples. The red colored box indicates the positively labeled ground truth region, while the green colored regions are detection results of the DGCA-RCNN framework.

4. Discussion

4.1. The main findings of the study

The most important findings of our study are as follows: (1). There are currently few network architectures designed specifically for cervical cancer cell detection in Pap smear images[42,44-46]. Based on one of the currently top-performing detectors faster RCCN-FPN[57] and the characteristics of the cervical smear images, we proposed a novel DGCA-RCNN framework. Experimental results based on an openly accessible contest dataset of WSIs have demonstrated that the proposed architecture outperforms all other state-of-the-art models; (2) Tagging the negative samples with traditional computer-vision imaging techniques can reinforce the subtle and complex contrasts between the normal and abnormal cervical cells and reduce false positive detections; (3) Introducing deformable convolutional layers into the feature extraction pyramid network can improve scalability of the model and detection of deformed cells of various sizes; (4) Besides morphological and textural features, spatial context information can also be relevant for the detection of abnormal cells. Infusing context aware module into the detector can contribute positively to the performance of the framework.

4.2 Image magnification and IOU threshold

Detection of small cells in images is a challenging task due to the relatively small area with limited information. The Faster RCNN-FPN based architecture leverages the multiscale feature hierarchy to detect objects of various sizes[57]. For small objects there is little information left on the top-most feature map, which may compromise the detection of the small cells. FPN makes full use of the pyramidal feature maps by building a top-down pathway with lateral connections to the corresponding bottom-up feature maps, which significantly improves its detection accuracy compared with conventional detectors. Nevertheless, the features from the bottom levels have weak semantic information and could harm their representational capacity for small object recognition. As the system progressively reduces the input images to smaller feature maps at top levels, it retains little spatial information of small objects. Therefore, it is difficult to restore the lost details of small objects by up-sampling in the top-down route. Moreover, the combination of the low- and high-level features plays an important role in object detection. In the Faster RCNN-FPN based architectures feature maps of the 2 pathways

Preprints (www.preprints.org) | NOT PEER-REVIEWED | Posted: 12 July 2021 doi:10.20944/preprints202107.0277.v1

are added in a simple fashion. Such direct feature combination may result in background clutter and semantic ambiguity.

In this study we used WSIs of 20x and the cells are relatively small. As discussed above, Images with higher magnification are strongly favorable for the detection of cervical cancerous cells. A recent study[44] based on the Faster RCNN model used TCT images of 400x and achieved AUC=0.67 with IOU threshold=0.5. which is about 12% higher than the result obtained in this study for the similar model (Faster RCNN-FPN) and IOU. It is reasonable to attribute the difference to the magnification difference of the input WSIs. The basal diploids in cervical Pap smear images have large variations in size and tend to form clumps. Microscopic examinations are usually conducted at 200x to magnify the subtle feature differences between cells. Under low magnification as the dataset used in this study, the occupancy of the cells in an image patch is relatively small. The precise localization of the cells becomes quite challenging. A previous study suggested an interesting concept to alleviate this by counting any overlap between a ground truth box and the detection result as a true hit irrespective of the IOU threshold. In this study, we assessed the performance of the detector at 3 different IOU thresholds (0.1, 0.3 and 0.5). It is notable that mAP decreased from 0.505 to 0.445 on when IOU was increased from 0.1 to 0.5. To facilitate accurate detection of cancerous cells, it is desirable to acquire sufficiently magnified image patches where the targeted cells occupy a significant fraction of the image, because details are required for the detector to automatically learn the subtle features and use them to detect the targeted cells. Partially obscured cells can be also identified if sufficient pixels are present. If the cells in the image patches appear too small, the detector's performance may degrade to a point that the cells are miss-classified or missed entirely. Very little research has been done to determine the performance limits for object detection algorithms when the object size is reduced[58,59]. Other limitations in image qualities[59], such as blurring, noise, contrast, and lossy compression are even less known.

4.3. Limited train dataset and unlabeled cells

The lack of train dataset is one of the main obstacles to develop machine learning methods for automated cervical cancer cell detection in cytology images because of privacy integrity and labeling cost issues[60]. A collection of at least hundreds of high-quality, well-curated digitized images of Pap smears and associated cell annotation results are required to train a machine learning model. The openly accessible Pap smears image database is currently quite limited and without balanced representation for cell types of pre-neoplastic alteration. As summarized in Table 7, the currently available datasets are mostly composed of cut-out cell images.

Table 7. Summary of the openly accessible Pap smear image datasets in the literature.

Property	CRIC Cervix [60]	Herlev [27]	SIPakMed [61]	DHB
Images (n)	400	917	966	500/300
Cells per image	multiple	1	multiple	many
Image type	Cut-out cluster	Single cell	Isolated cells	WSI
Image size	1,376 × 1,020	variable	2,048 × 1,536	40,000x40,000
Resolution	0.228 μm/pixel	0.201μm/pixel	unknown	20x
Classified Cells	11,534	917	4,049	5414

Preprints (www.preprints.org) | NOT PEER-REVIEWED | Posted: 12 July 2021 doi:10.20944/preprints202107.0277.v1

Validation source	3 cytologists database.cric.com.br	2 cytologists mde-lab.aegean.gr	cytologists cs.uoi.gr	Cytologists *

* tianchi.aliyun.com/competition/entrance/231757/information.

The Herlev dataset [27] is a widely used dataset for classification of cervical cancer cells. It consists of 917 single cell images, which have been categorized into 7 pre-neoplastic lesions by cervical cytology professionals. Other dataset used for Pap smear image classification studies includes the SIPaKMeD database[61] consisting of 4,049 annotated cells in 966 cut-out images. The cells have been manually classified into five cell types without pre-neoplastic alteration by expert cytopathologists. Some previous studies have relied on image collections of cut-out images[41,43] of clean images or positive samples[42]. Despite of the seemingly good performance, these results are not so realistic and clinically relevant.

The classification of single cell images and detection of cervical cancerous cells in WSIs are quite different tasks. The latter is more challenging because it requires not only classification of the recognized abnormal lesions but also the identification and localization of the abnormal cervical cells in WSIs. Unlike the cut-out singe cell images, WSIs from cervical cancer screening tests have a broad diversity of neoplastic lesions and many other challenges, including image quality issues discussed above, overlapping cells and inflammatory cells. Moreover, the datasets to train a detection model need to provide the ground-truth locations and size of the cancerous lesions and such datasets are rarely available. To the best of our knowledge, the DHB dataset used in the current study is the only cervical Pap smear WSI dataset labeled for cancer cell detection. Besides the relatively low magnification issued discussed above, there are number of important limitation factors associated with the dataset, which can significantly influence the detection performance. Firstly, the lesions were not exhaustively labeled and there is no guarantee that the cells outside the tagged regions are all normal. This means that false positive detections outside the tagged regions can be true positive, and the detection performance can, therefore, be underestimated. Secondly, the occupancy of the labeled regions was only a small fraction (<1ppm) of the WSI images. This implies that the relative populations between the abnormal and normal cells are substantially out of balance (in the order of 104) and the clinical relevance of the detection algorithm should focus on reducing false negative detections. During model training, we attempted to balance the positive and negative labeled samples (see Table 2). Therefore, there are substantial fraction of cells are unlabeled both in the negative and positive samples. Considering the potentially large number and wide diversity of object instances in Pap Smear WSIs, it is inherently a challenging task to constitute complete exhaustive annotations. The missing annotations can be problematic, as the standard cross-entropy loss employed to train the model implicitly treats the unlabeled regions as background. Any unlabeled object (without a bounding box) can result in a confusing learning signal[62]. This can be addressed by removing the assumption that unlabeled regions must be background.

5. Conclusions

In this study, we proposed a novel DGCA-RCNN framework for the detection of abnormal cervical cells in Pap smear images. We extended the Faster RCNN-FPN model by introducing deformable convolution layers into FPN to improve scalability and

adding a GCA module alongside RPN to enhance the spatial context information. The results from extensive experiments have demonstrated that the proposed model has significant improved mAP and AUC for the detection of abnormal cells in Pap smear WSIs and outperform other state-of-art detectors. When combined with tagging of the negative image samples using computer-vision techniques, 6-9% increase in mAP has been achieved. The main limiting factors include WSI magnification and adequate labeling. The proposed DGCA-RCNN model has great potential to become a clinically useful AI tool for automated detection of cervical cancer cells in Pap smear images.

Author Contributions: Conceptualization, X.L., Z.X., X.S. and T.L.; Data curation, X.S.; Formal analysis, Z.X., X.S. and T.L.; Funding acquisition, X.L. and T.L.; Investigation, Z.X. and Y.Z.; Methodology, Z.X., X.S. and B.X.; Project administration, X.L.; Resources, X.L.; Software, Z.X., X.S. and B.X.; Supervision, X.L.; Validation, Y.Z. and B.X.; Visualization, Y.Z. and B.X.; Writing – original draft, X.L., Z.X. and X.S.; Writing – review & editing, X.L., Y.Z. and T.L.

Funding: This research was funded by China Scholarship Council, Zhejiang Natural Science Foundation, grant number LY18E070005 and Key Research and Development Program of Zhejiang Province, grant number 2020C03020.

Institutional Review Board Statement: Not applicable.

Informed Consent Statement: Patient consent was waived due to the image data were obtained from an openly accessible source.

Data Availability Statement: The image data used in the study are openly accessible at the following site: https://tianchi.aliyun.com/competition/entrance/231757/introduction.

Conflicts of Interest: The authors declare no conflict of interest.

References

1. Arbyn, M.; Weiderpass, E.; Bruni, L.; de Sanjosé, S.; Saraiya, M.; Ferlay, J.; Bray, F. Estimates of incidence and mortality of cervical cancer in 2018: a worldwide analysis. *The Lancet Global Health* **2020**, *8*, e191-e203, doi:10.1016/s2214-109x(19)30482-6.
2. Thrall, M.J. Automated screening of Papanicolaou tests: A review of the literature. *Diagn Cytopathol* **2019**, *47*, 20-27, doi:10.1002/dc.23931.
3. Zhang, L.; Kong, H.; Ting Chin, C.; Liu, S.; Fan, X.; Wang, T.; Chen, S. Automation-assisted cervical cancer screening in manual liquid-based cytology with hematoxylin and eosin staining. *Cytometry A* **2014**, *85*, 214-230, doi:10.1002/cyto.a.22407.
4. Birdsong, G.G. Automated screening of cervical cytology specimens. *Hum Pathol* **1996**, *27*, 468-481, doi:10.1016/s0046-8177(96)90090-8.
5. Bengtsson, E.; Malm, P. Screening for cervical cancer using automated analysis of PAP-smears. *Comput Math Methods Med* **2014**, *2014*, 842037, doi:10.1155/2014/842037.
6. Song, Y.; Zhang, L.; Chen, S.; Ni, D.; Lei, B.; Wang, T. Accurate Segmentation of Cervical Cytoplasm and Nuclei Based on Multiscale Convolutional Network and Graph Partitioning. *IEEE Trans Biomed Eng* **2015**, *62*, 2421-2433, doi:10.1109/tbme.2015.2430895.
7. Zhang, L.; Le, L.; Nogues, I.; Summers, R.M.; Liu, S.; Yao, J. DeepPap: Deep Convolutional Networks for Cervical Cell Classification. *IEEE J Biomed Health Inform* **2017**, *21*, 1633-1643, doi:10.1109/JBHI.2017.2705583.
8. Chankong, T.; Theera-Umpon, N.; Auephanwiriyakul, S. Automatic cervical cell segmentation and classification in Pap smears. *Comput Methods Programs Biomed* **2014**, *113*, 539-556, doi:10.1016/j.cmpb.2013.12.012.
9. Chen, Y.F.; Huang, P.C.; Lin, K.C.; Lin, H.H.; Wang, L.E.; Cheng, C.C.; Chen, T.P.; Chan, Y.K.; Chiang, J.Y. Semi-automatic segmentation and classification of Pap smear cells. *IEEE J Biomed Health Inform* **2014**, *18*, 94-108, doi:10.1109/jbhi.2013.2250984.
10. Guan, T.; Zhou, D.; Liu, Y. Accurate segmentation of partially overlapping cervical cells based on dynamic sparse contour searching and GVF snake model. *IEEE J Biomed Health Inform* **2015**, *19*, 1494-1504, doi:10.1109/jbhi.2014.2346239.

11. Lu, Z.; Carneiro, G.; Bradley, A.P.; Ushizima, D.; Nosrati, M.S.; Bianchi, A.G.C.; Carneiro, C.M.; Hamarneh, G. Evaluation of Three Algorithms for the Segmentation of Overlapping Cervical Cells. *IEEE J Biomed Health Inform* **2017**, *21*, 441-450, doi:10.1109/jbhi.2016.2519686.
12. Yang-Mao, S.F.; Chan, Y.K.; Chu, Y.P. Edge enhancement nucleus and cytoplast contour detector of cervical smear images. *IEEE Trans Syst Man Cybern B Cybern* **2008**, *38*, 353-366, doi:10.1109/tsmcb.2007.912940.
13. Zhang, L.; Kong, H.; Chin, C.T.; Liu, S.; Chen, Z.; Wang, T.; Chen, S. Segmentation of cytoplasm and nuclei of abnormal cells in cervical cytology using global and local graph cuts. *Comput Med Imaging Graph* **2014**, *38*, 369-380, doi:10.1016/j.compmedimag.2014.02.001.
14. Zhang, L.; Kong, H.; Liu, S.; Wang, T.; Chen, S.; Sonka, M. Graph-based segmentation of abnormal nuclei in cervical cytology. *Comput Med Imaging Graph* **2017**, *56*, 38-48, doi:10.1016/j.compmedimag.2017.01.002.
15. Plissiti, M.E.; Nikou, C. Overlapping cell nuclei segmentation using a spatially adaptive active physical model. *IEEE Trans Image Process* **2012**, *21*, 4568-4580, doi:10.1109/tip.2012.2206041.
16. Ali, S.; Madabhushi, A. An integrated region-, boundary-, shape-based active contour for multiple object overlap resolution in histological imagery. *IEEE Trans Med Imaging* **2012**, *31*, 1448-1460, doi:10.1109/tmi.2012.2190089.
17. Kong, H.; Gurcan, M.; Belkacem-Boussaid, K. Partitioning histopathological images: an integrated framework for supervised color-texture segmentation and cell splitting. *IEEE Trans Med Imaging* **2011**, *30*, 1661-1677, doi:10.1109/tmi.2011.2141674.
18. Song, Y.; Tan, E.L.; Jiang, X.; Cheng, J.Z.; Ni, D.; Chen, S.; Lei, B.; Wang, T. Accurate Cervical Cell Segmentation from Overlapping Clumps in Pap Smear Images. *IEEE Trans Med Imaging* **2017**, *36*, 288-300, doi:10.1109/tmi.2016.2606380.
19. Iliyasu, A.M.; Fatichah, C. A Quantum Hybrid PSO Combined with Fuzzy k-NN Approach to Feature Selection and Cell Classification in Cervical Cancer Detection. *Sensors (Basel)* **2017**, *17*, doi:10.3390/s17122935.
20. Esteva, A.; Kuprel, B.; Novoa, R.A.; Ko, J.; Swetter, S.M.; Blau, H.M.; Thrun, S. Dermatologist-level classification of skin cancer with deep neural networks. *Nature* **2017**, *542*, 115-118, doi:10.1038/nature21056.
21. Li, X.; Shen, X.; Zhou, Y.; Wang, X.; Li, T.Q. Classification of breast cancer histopathological images using interleaved DenseNet with SENet (IDSNet). *PLoS One* **2020**, *15*, e0232127, doi:10.1371/journal.pone.0232127.
22. Savage, N. Another set of eyes for cancer diagnostics. *Nature* **2020**, *579*, s14-s16.
23. Ardila, D.; Kiraly, A.P.; Bharadwaj, S.; Choi, B.; Reicher, J.J.; Peng, L.; Tse, D.; Etemadi, M.; Ye, W.; Corrado, G.; et al. End-to-end lung cancer screening with three-dimensional deep learning on low-dose chest computed tomography. *Nat Med* **2019**, *25*, 954-961, doi:10.1038/s41591-019-0447-x.
24. Skrede, O.-J.; De Raedt, S.; Kleppe, A.; Hveem, T.S.; Liestøl, K.; Maddison, J.; Askautrud, H.A.; Pradhan, M.; Nesheim, J.A.; Albregtsen, F.; et al. Deep learning for prediction of colorectal cancer outcome: a discovery and validation study. *The Lancet* **2020**, *395*, 350-360, doi:10.1016/s0140-6736(19)32998-8.
25. Ashok B, a.A.P. Comparison of Feature selection methods for diagnosis of cervical cancer using SVM classifier. *Int. J. Eng. Res. Appl* **2016**, *6*, 99-104.
26. Bora, K.; Chowdhury, M.; Mahanta, L.B.; Kundu, M.K.; Das, A.K. Pap smear image classification using convolutional neural network. In Proceedings of the the Tenth Indian Conference on Computer Vision, Graphics and Image Processing - ICVGIP '16, Guwahati, India, 2016; pp. 1-8.
27. Jantzen, J., Norup, J., Dounias, G., & Bjerregaard, B. Pap-smear Benchmark Data For Pattern Classification. . In Proceedings of the Nature inspired Smart Information Systems : EU co-ordination action, Albufeira, Portugal, 2005; pp. 1-9.
28. Lu, Z.; Carneiro, G.; Bradley, A.P. Automated nucleus and cytoplasm segmentation of overlapping cervical cells. *Med Image Comput Comput Assist Interv* **2013**, *16*, 452-460, doi:10.1007/978-3-642-40811-3_57.
29. Nirmal Jith, O.U.; Harinarayanan, K.K.; Gautam, S.; Bhavsar, A.; Sao, A.K. DeepCerv: Deep Neural Network for Segmentation Free Robust Cervical Cell Classification. In *Computational Pathology and Ophthalmic Medical Image Analysis*; Lecture Notes in Computer Science; 2018; pp. 86-94.

30. Sokouti, B.; Haghipour, S.; Tabrizi, A.D. A framework for diagnosing cervical cancer disease based on feedforward MLP neural network and ThinPrep histopathological cell image features. *Neural Computing and Applications* **2012**, *24*, 221-232, doi:10.1007/s00521-012-1220-y.
31. Wu, W.; Zhou, H. Data-Driven Diagnosis of Cervical Cancer With Support Vector Machine-Based Approaches. *IEEE Access* **2017**, *5*, 25189-25195, doi:10.1109/access.2017.2763984.
32. Cai, Z.; Vasconcelos, N. Cascade R-CNN: High Quality Object Detection and Instance Segmentation. *IEEE Trans Pattern Anal Mach Intell* **2021**, *43*, 1483-1498, doi:10.1109/tpami.2019.2956516.
33. Lin, T.; Dollár, P.; Girshick, R.; He, K. Feature pyramid networks for object detection. In Proceedings of the the IEEE conference on computer vision and pattern recognition, Las Vegas, NV, USA, 2017; pp. 2117-2126.
34. Ren, S.; He, K.; Girshick, R.; al, e. Faster R-CNN: Towards real-time object detection with region proposal networks. *Advances in neural information processing systems.* **2015**, 91-99, doi:10.1007/s11263-013-0620-5.
35. Ren, S.; He, K.; Girshick, R.; Sun, J. Faster R-CNN: Towards Real-Time Object Detection with Region Proposal Networks. *IEEE Trans Pattern Anal Mach Intell* **2017**, *39*, 1137-1149, doi:10.1109/TPAMI.2016.2577031.
36. Jiang, X.; Zeng, Y.; Xiao, S.; He, S.; Ye, C.; Qi, Y.; Zhao, J.; Wei, D.; Hu, M.; Chen, F. Automatic Detection of Coronary Metallic Stent Struts Based on YOLOv3 and R-FCN. *Comput Math Methods Med* **2020**, *2020*, 1793517, doi:10.1155/2020/1793517.
37. Redmon J, D.S., Girshick R, et al. . You only look once: Unified, real-time object detection. In Proceedings of the 2016 IEEE Conference on Computer Vision and Pattern Recognition (CVPR), Las Vegas, NV, USA, 2016; pp. 779-788.
38. Liu, W.; Anguelov, D.; Erhan, D.e.a. Single shot multibox detector. *European conference on computer vision. Springer, Cham* **2016**, 17, doi:10.1007/978-3-642-40811-3_57.
39. Lin, T.Y.; Goyal, P.; Girshick, R.; He, K.; Dollar, P. Focal Loss for Dense Object Detection. *IEEE Trans Pattern Anal Mach Intell* **2020**, *42*, 318-327, doi:10.1109/tpami.2018.2858826.
40. Li, H.; Zhao, S.; Zhao, W.; Zhang, L.; Shen, J. One-Stage Anchor-Free 3D Vehicle Detection from LiDAR Sensors. *Sensors (Basel)* **2021**, *21*, 2651-2668, doi:10.3390/s21082651.
41. Bhatt, A.R.; Ganatra, A.; Kotecha, K. Cervical cancer detection in pap smear whole slide images using convNet with transfer learning and progressive resizing. *PeerJ Comput Sci* **2021**, *7*, e348, doi:10.7717/peerj-cs.348.
42. Ma, D.; Liu, J.; Li, J.; Zhou, Y. Cervical cancer detection in cervical smear images using deep pyramid inference with refinement and spatial-aware booster. *IET Image Processing* **2021**, *14*, 4717-4725, doi:10.1049/iet-ipr.2020.0688.
43. Rahaman, M.M.; Li, C.; Wu, X.; Yao, Y.; Hu, Z.; Jiang, T.; Li, X.; Qi, S. A Survey for Cervical Cytopathology Image Analysis Using Deep Learning. *IEEE Access* **2020**, *8*, 61687-61710, doi:10.1109/access.2020.2983186.
44. Tan, X.; Li, K.; Zhang, J.; Wang, W.; Wu, B.; Wu, J.; Li, X.; Huang, X. Automatic model for cervical cancer screening based on convolutional neural network: a retrospective, multicohort, multicenter study. *Cancer Cell Int* **2021**, *21*, 35-44, doi:10.1186/s12935-020-01742-6.
45. Xu, M.; Zeng, W.; Sun, Y.; Wu, H.; Wu, T.; Yang, Y.; Zhang, M.; Zhu, Z.; Chen, L. Cervical cytology intelligent diagnosis based on object detection technology. In Proceedings of the 1st Conference on Medical Imaging with Deep Learning (MIDL 2018), Amsterdam, The Netherlands, Jan 7, 2018; pp. 1-9.
46. Zhang, J.; He, J.; Chen, T.; Liu, Z.; Chen, D. Abnormal region detection in cervical smear images based on fully convolutional network. *IET Image Processing* **2019**, *13*, 583-590, doi:10.1049/iet-ipr.2018.6032.
47. Peng, J.; Bao, C.; Hu, C.; Wang, X.; Jian, W.; Liu, W. Automated mammographic mass detection using deformable convolution and multiscale features. *Med Biol Eng Comput* **2020**, *58*, 1405-1417, doi:10.1007/s11517-020-02170-4.
48. Deng, L.; Chu, H.-H.; Shi, P.; Wang, W.; Kong, X. Region-Based CNN Method with Deformable Modules for Visually Classifying Concrete Cracks. In Proceedings of the 2017 IEEE Conference on Computer Vision and Pattern Recognition (CVPR), Honolulu, HI, USA, July 21st, 2020; pp. 2528-2545.
49. Cao, D.; Chen, Z.; Gao, L. An improved object detection algorithm based on multi-scaled and deformable convolutional

neural networks. *Human-centric Computing and Information Sciences* **2020**, *10*, 14-35, doi:10.1186/s13673-020-00219-9.

50. Siddiqui, S.A.; Malik, M.I.; Agne, S.; Dengel, A.; Ahmed, S. DeCNT: Deep Deformable CNN for Table Detection. *IEEE Access* **2018**, *6*, 74151-74161, doi:10.1109/access.2018.2880211.
51. Ren, Y.; Zhu, C.; Xiao, S. Deformable Faster R-CNN with Aggregating Multi-Layer Features for Partially Occluded Object Detection in Optical Remote Sensing Images. *Remote Sensing* **2018**, *10*, doi:10.3390/rs10091470.
52. Xiao, Y.; Wang, X.; Zhang, P.; Meng, F.; Shao, F. Object Detection Based on Faster R-CNN Algorithm with Skip Pooling and Fusion of Contextual Information. *Sensors (Basel)* **2020**, *20*, doi:10.3390/s20195490.
53. Zhang, S.; Chi, C.; Yao, Y.; Lei, Z.; Li, S.Z. Bridging the gap between anchor-based and anchor-free detection via adaptive training sample selection. In Proceedings of the the IEEE/CVF Conference on Computer Vision and Pattern Recognition, Virtual, June 16th, 2020; pp. 9759-9768.
54. Wu, Y.; Chen, Y.; Yuan, L.; Liu, Z.L.; Wang, L.; Li, H.; Fu, Y. Rethinking Classification and Localization for Object Detection. In Proceedings of the the IEEE/CVF Conference on Computer Vision and Pattern Recognition., Virtual, 2020; pp. pp. 10186-11095.
55. Dai, J.; Qi, H.; Xiong, Y.; Li, Y.; Zhang, G.; Hu, H.; Wei, Y. Deformable convolutional networks. In Proceedings of the 2017 IEEE Conference on Computer Vision and Pattern Recognition (CVPR), Honolulu, HI, USA, July 21st, 2017; pp. 764-773.
56. He, K.; Zhang, X.; Ren, S.; Sun, J. Deep residual learning for image recognition. In Proceedings of the 2016 IEEE Conference on Computer Vision and Pattern Recognition (CVPR), Las Vegas, NV, USA, June 27, 2016; pp. 770-778.
57. Cao, C.; Wang, B.; Zhang, W.; Zeng, X.; Yan, X.; Feng, Z.; Liu, Y.; Wu, Z. An Improved Faster R-CNN for Small Object Detection. *IEEE Access* **2019**, *7*, 106838-106846, doi:10.1109/access.2019.2932731.
58. Boom, B.J.; Beumer, G.M.; Spreeuwers, L.J.; Veldhuis, R.N.J. The Effect of Image Resolution on the Performance of a Face Recognition System. In Proceedings of the 2006 9th International Conference on Control, Automation, Robotics and Vision, Singapore, December 5th, 2006; pp. 1-6.
59. Cui, L.; Ma, R.; Lv, P.; Jiang, X.; gao, Z.; Zhou, B.; Xu, M. MDSSD: Multi-scale Deconvolutional Single Shot Detector for Small Objects. *Sci China Info Sci* **2020**, *63*, 120113-120115, doi:0.1007/s11432-019-2723-1.
60. Rezende, M.T.; Silva, R.; Bernardo, F.O.; Tobias, A.H.G.; Oliveira, P.H.C.; Machado, T.M.; Costa, C.S.; Medeiros, F.N.S.; Ushizima, D.M.; Carneiro, C.M.; et al. Cric searchable image database as a public platform for conventional pap smear cytology data. *Sci Data* **2021**, *8*, 151, doi:10.1038/s41597-021-00933-8.
61. Plissiti, M.E.; Dimitrakopoulos, P.; Sfikas, G.; Nikou, C.; Krikoni, O.; Charchanti, A. Sipakmed: A New Dataset for Feature and Image Based Classification of Normal and Pathological Cervical Cells in Pap Smear Images. In Proceedings of the 2018 IEEE International Conference on Image Processing (ICIP), Athens, Greece, October 7th, 2018; pp. 3144-3148.
62. Yang, Y.; Liang, K.J.; Carin, L. Object Detection as a Positive-Unlabeled Problem. *ArXiv* **2020**, *abs/2002.04672*.